Electronic Supplementary Material (ESI) for Chemical Communications.
This journal is © The Royal Society of Chemistry 2020

Supporting Information

Self-derivation-behaviour of substrate realizing enhanced oxygen evolution reaction

Derun Li, ‡ [a,e] Zhongqin Pan, ‡ [a,b] Han Tao,[c] Jiachen Li,[d] Weishi Gu,[a] Baotong Li,[a,e] Chenglin Zhong,[f] Qiyu Jiang,[a] Changqing Ye,[a] and Qingwen Zhou*[a]

[a] School of Public Health, Nantong University, Jiangsu 226019, China.

*E-mail: qw_zhou@ntu.edu.cn

[b] State Key Laboratory of Analytical Chemistry for Life Sciences, School of Chemistry and Chemical Engineering, Nanjing University, Jiangsu 210023, China

[c] High School Affiliated To Nantong University, Jiangsu 226019, China.

[d] School of Chemical Engineering, Northwest University, Shaanxi 710069, China

[e] Angstrom Advanced Inc. (Angstrom), MA 02072, USA.

[f] National Laboratory of Solid State Microstructures, College of Engineering and Applied Sciences, and Collaborative Innovation Center of Advanced Microstructures, Nanjing University, Jiangsu 210093, China.

‡ These authors contributed equally to this work.

Experimental section

Chemicals

All reagents were of analytical grade and used without further purification. NiFe foam (labeled as NFF), Ni foam (labeled as NF), Fe foam (labeled as FF), and Cu foam (labeled as CF) were purchased from Suzhou Jiashide Co., Ltd.. Stainless steel mesh (labeled as SSM) was purchased from Anping Shenbo Wire Mesh Manufacture Co., Ltd.. Sodium hydroxide, potassium hydroxide, and hydrogen peroxide (30 wt.% in H_2O) were purchased from Shanghai Meryer Chemical Technology Co. Ltd.. Commercial RuO_2 nanoparticles were obtained from Alfa Aesar. Hydrochloric acid, ethanol, and acetone were purchased from Beijing Chemical Works. Nafion perfluorinated resin solution (5 wt%) were purchased from Shanghai Hesen Electric Co., Ltd.. Milli-Q deionized water (resistance of 18.2 MΩ cm at 25 °C) were used for all experiments.

Preparation of *sd*-NFF

NFF (10×40 mm, 1 mm in thickness) was first soaked in 3.0 M HCl for 10 min, then ultrasonically cleaned in ethanol, acetone, and deionized water, respectively, for 30 min in both steps prior to use. A piece of pretreated NFF was placed in a Teflon lined stainless autoclave (100 mL) containing 30 mL aqueous solution (0.12 g NaOH, 750 μL H_2O_2). The autoclave was sealed and maintained at 150 °C for 6 h in an electric oven. After the autoclave cooled down slowly to room temperature, the sample was taken out and washed with water and ethanol thoroughly before drying. The loading mass of NiFe LDH nanosheets on NFF was calculated to be ~0.23 mg cm^{-2} by use of the flame atomic absorption spectrometry (FAAS) analysis reported in a previous work.[1] A series of *sd*-NFF samples were also prepared under the same hydrothermal conditions using different amount of H_2O_2 (0, 500 μL, and 1000 μL).

Preparation of *sd*-NF, *sd*-FF, *sd*-SSM, and *sd*-CF

sd-NF, *sd*-FF, *sd*-SSM, and *sd*-CF were prepared using the same method as *sd*-NFF, except that the NFF substrate was replaced by NF, FF, SSM, and CF, respectively.

Preparation of RuO_2@NFF

5 mg RuO_2 powder and 32 μL of 5 wt.% Nafion solution were dispersed in 0.968 mL of 4:1 (V/V) water/ethanol by sonication for at least 30 min to form a homogeneous ink. Then 50 μL of the catalyst ink (containing 0.25 mg of RuO_2 catalyst) was loaded onto a 1×1 cm NFF.

Characterizations

The phase compositions of the catalysts were characterized by x-ray diffraction (XRD, Rigaku SmartLab, operated at 40 kV and 44 mA, parallel beam mode, λ=1.54 Å, step size 0.01 degree and scan rate 1 degree/min). Flame atomic absorption spectrometry (FAAS, Z-2000, Hitachi) was used for the determination of the content of dissolved Ni, Fe residue in the synthesis process. Morphology observation and energy dispersive X-ray (EDX) spectrum analysis were conducted using a Zeiss Ultra 55 field emission scanning electron microscope (SEM). Transmission electron microscopy (TEM) characterization and selected area electron diffraction (SAED) pattern were obtained using an FEI Tecnai G2 20 microscope at 200 kV. X-ray photoelectron spectroscopy (XPS) analysis was performed on an ESCALab MKII spectrometer with Mg Ka X-ray as the excitation source. Fourier transform infrared spectra (FTIR) were obtained on a Nicolet iS50 spectrophotometer. A Nano ZS90 Zetasizer analyzer (Malvern Instruments Ltd, UK) was used to measure the zeta potentials of surface catalysts on obtained electrodes. Quantitative analysis of elementary composition was carried out using inductively coupled plasma atomic emission spectroscopy (TJA RADIAL IRIS 1000 ICP-AES). Electron paramagnetic resonance (EPR) spectra were conducted on a JEOL JES-FA200 EPR spectrometer operating at room temperature with a microfrequency of 9.062 GHz.

Electrochemical Measurement

The electrochemical measurements were carried out in a three-electrode system through the electrochemical workstation (CHI 760E). Hg/HgO was used as the reference electrode and

carbon rod as the counter electrode. OER performances were measured through performing linear sweep voltammetry (LSV, scan rate of 2 mV s^{-1}) in O_2 saturated KOH (1.0 M) solution. All of the measured potentials (vs. Hg/HgO) were converted to the potentials against the reversible hydrogen electrode (RHE). Prior to the measurement, cyclic voltammograms (CV, -0.3 V to 0.5 V vs. RHE) were carried out at a scan rate of 20 mV s^{-1} for 20 cycles. The long-term durability test was performed using chronopotentiometric measurements. EIS data were collected at the overpotential of 280 mV (vs. RHE) from 100 kHz to 0.01 Hz with an AC amplitude of 10 mV. All potentials presented were corrected against ohmic potential drop with 85% *iR* compensation. The ECSA was characterized according to a reported method.[2, 3] Specifically, CV (50, 60, 70, 80, and 100 mV s^{-1}) were collected in a narrow potential window of 0.674 V to 0.774 V (vs. RHE) where no faradaic reactions occurred. The capacitive currents of $\Delta J|J_a-J_c|/2$ are plotted with respect to the CV scan rates. The slope of the fitted line is the double layer capacitance (C_{dl}), which is proportional to the surface area of the electrode. The ECSA was calculated according to the following equation:

$$ECSA=\frac{C_{dl}\times A}{C_{ref}}$$

where A is the geometric area of the electrode (1 cm^2 in our case), C_{ref} is the referential areal capacitance of flat electrode (40 μF cm^{-2} is used as suggested by the ref. [4, 5]).

Supplementary Figures

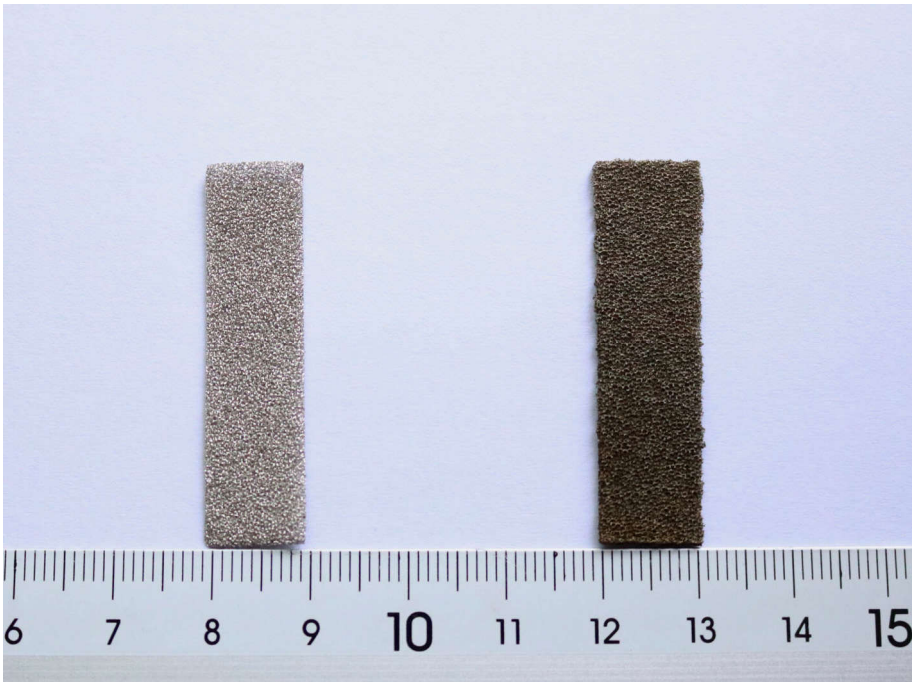

Fig. S1 Photograph of the bare NFF (left) and *sd*-NFF (right).

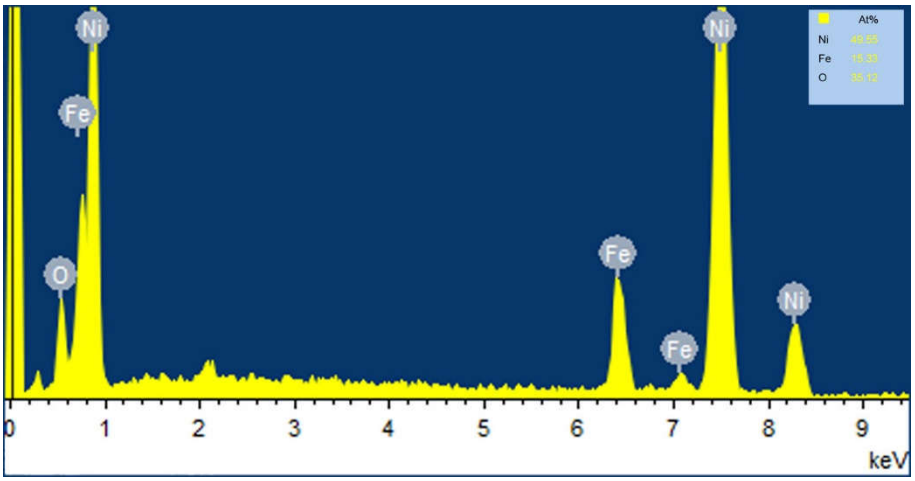

Fig. S2. EDX spectrum of the *sd*-NFF.

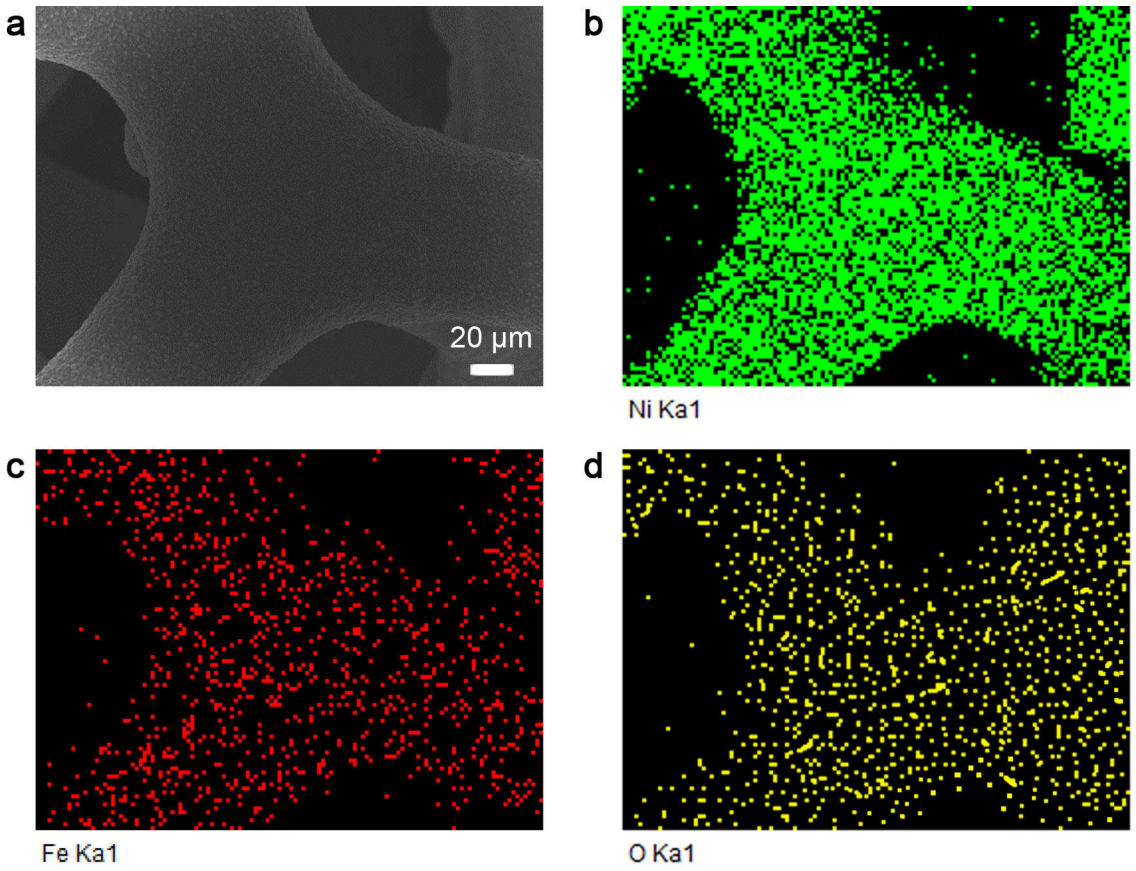

Fig. S3. (a) SEM image and the corresponding EDX elemental mapping images of (b) Ni, (c) Fe, and (d) O in the *sd*-NFF.

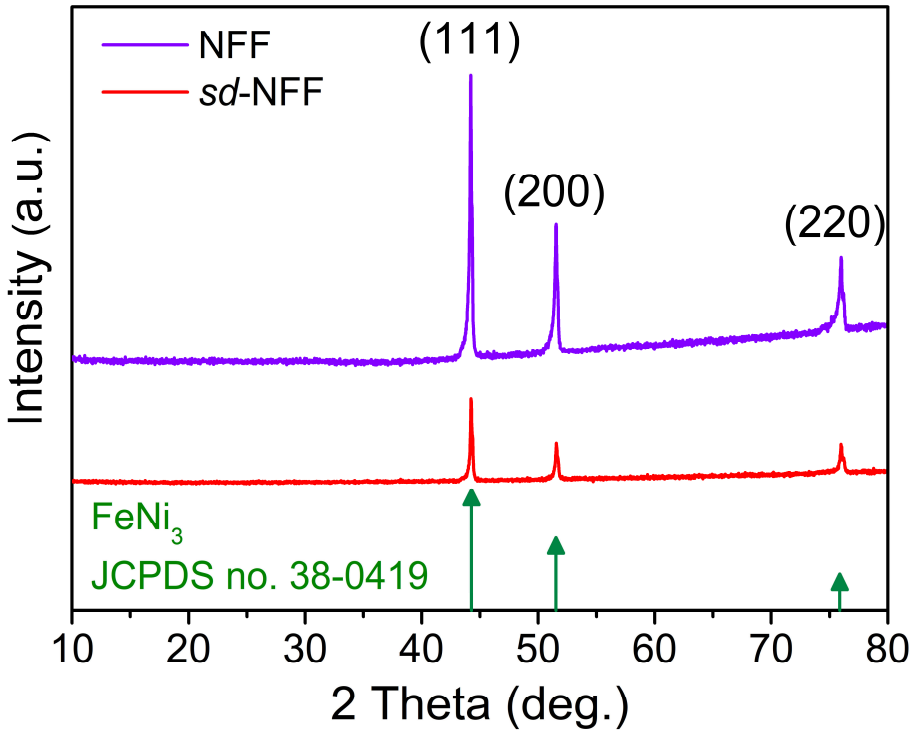

Fig. S4. XRD patterns of the pristine NFF and *sd*-NFF.

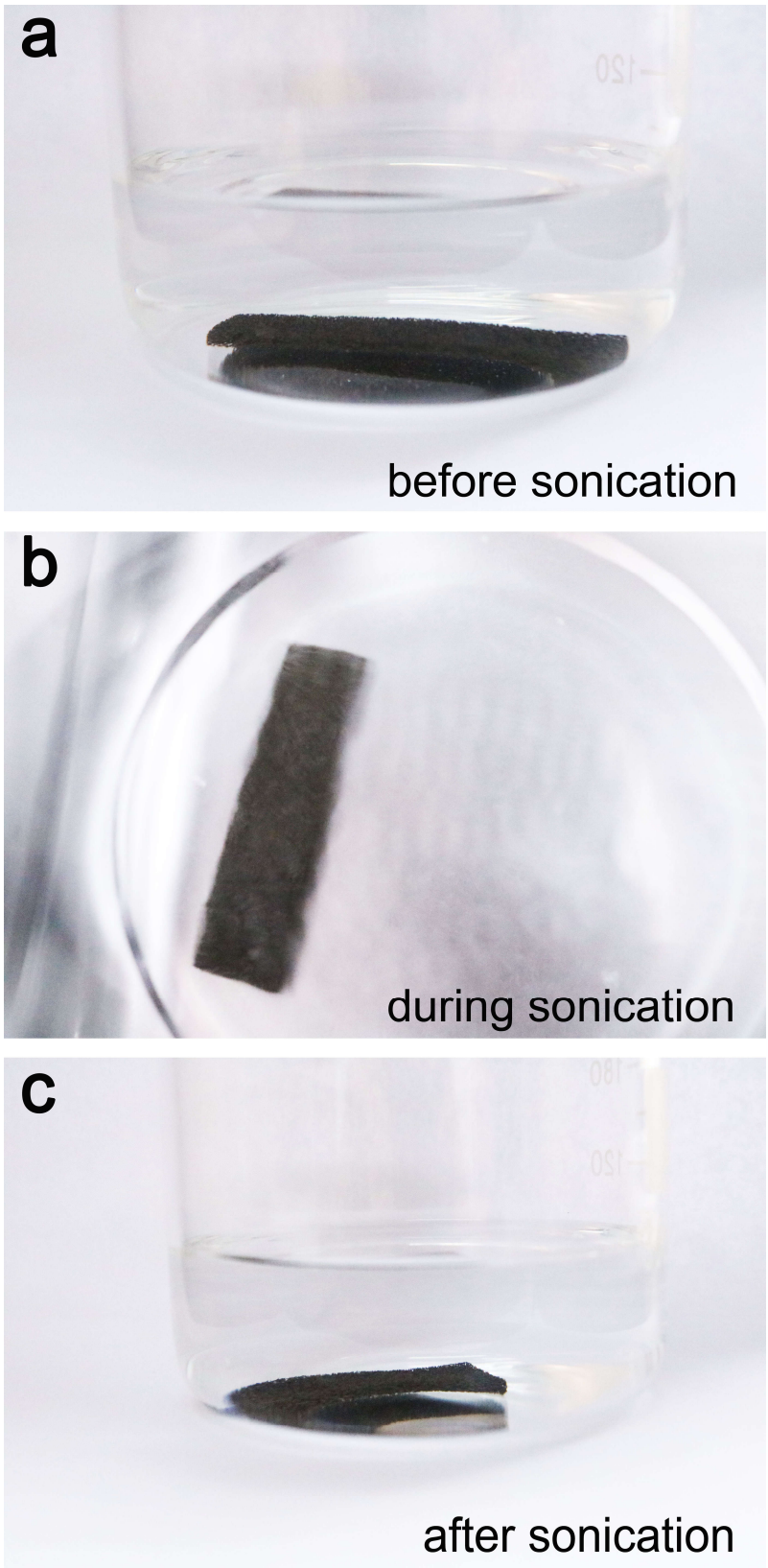

Fig. S5. Photographs of the as-prepared *sd*-NFF during 30 minutes sonication to monitor the mechanical stability of the catalyst layer: (a) before sonication, (b) during sonication, and (c) after sonication.

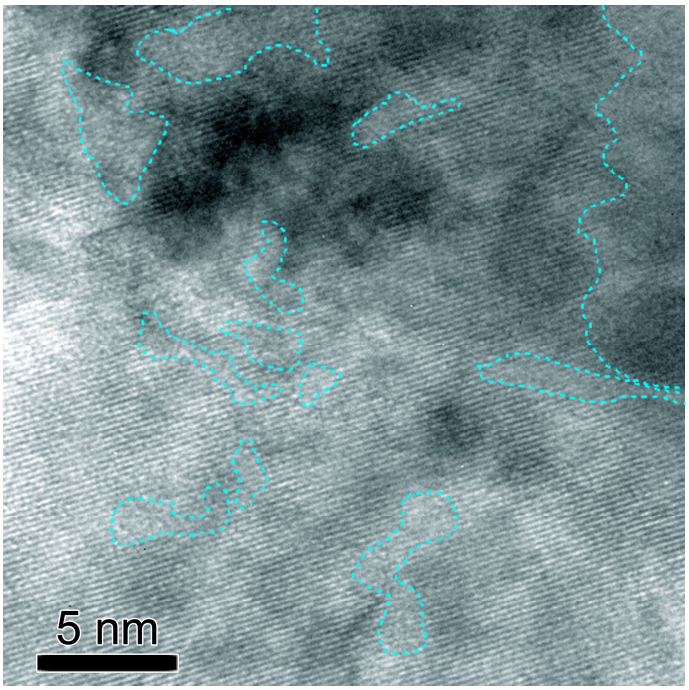

Fig. S6. High-resolution TEM image of NiFe LDH on *sd*-NFF, where lattice defects can be clearly revealed. Several defecttive regions were highlighted by dashed curves.

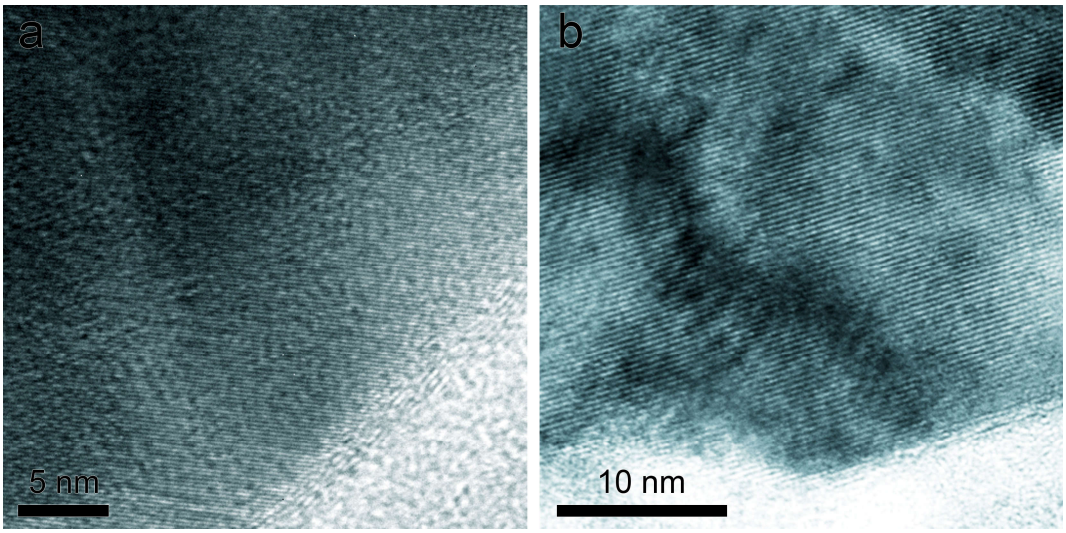

Fig. S7. High-resolution TEM image (a, b) of NiFe LDH on *sd*-NFF electrode prepared without adding H_2O_2.

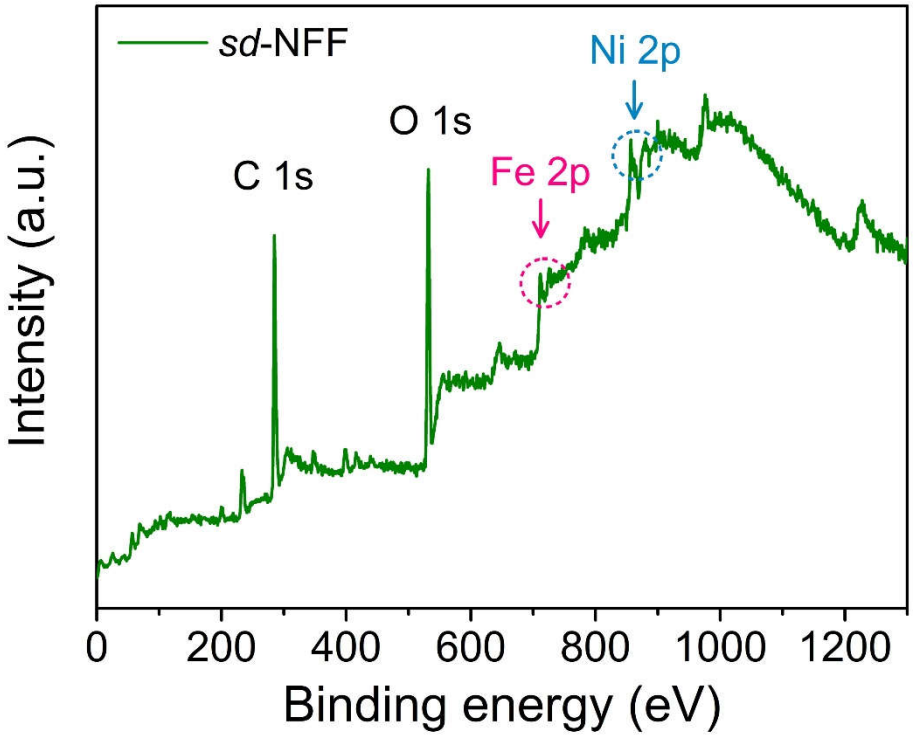

Fig. S8. XPS total spectrum of the *sd*-NFF.

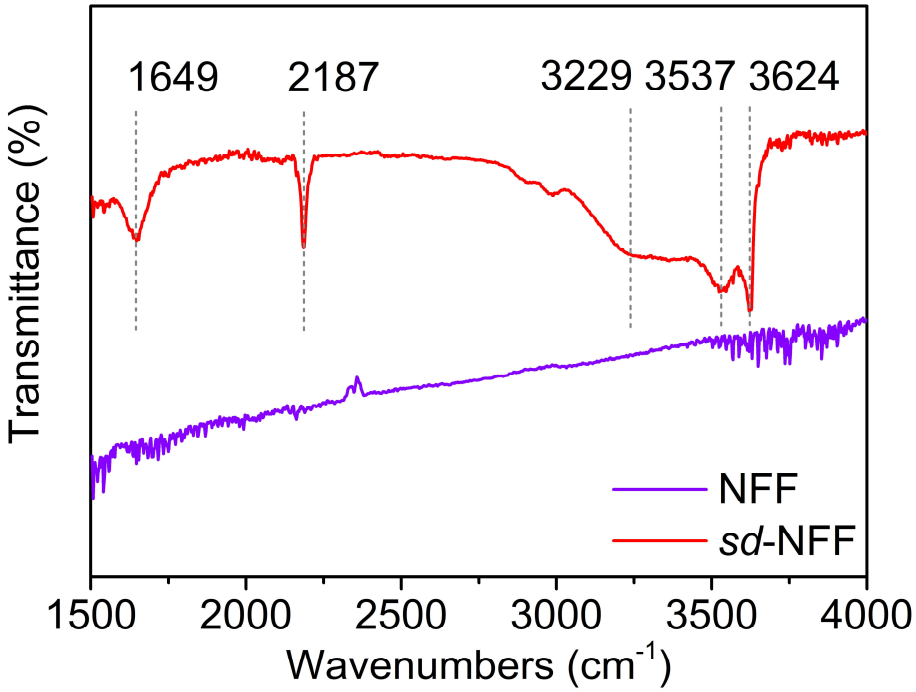

Fig. S9. FTIR spectra of the pristine NFF and *sd*-NFF.

The Fourier transform infrared spectroscopy (FTIR) analysis is used to further verify the formation of NiFe LDH. As can be seen from Fig. S9, FTIR spectra reveal that the broad peaks located at 1649, 3537, and 3229 cm^{-1} are the stretching of O-H groups of adsorbed free water.[6] The peaks at 3624 cm^{-1} is assigned to the O-H vibrations of NiFe LDH lattice.[7] The vibrational frequency at 2187 cm^{-1} is attributed to the intercalated carbonates in the NiFe LDH.[8] The formation of carbonates is probably due to the CO_2 in air (inside Teflon-lined stainless autoclave). Finally, no identifiable peaks can be found in the spectra of NFF, further evidencing the successful transformation of surface NiFe to NiFe LDH.

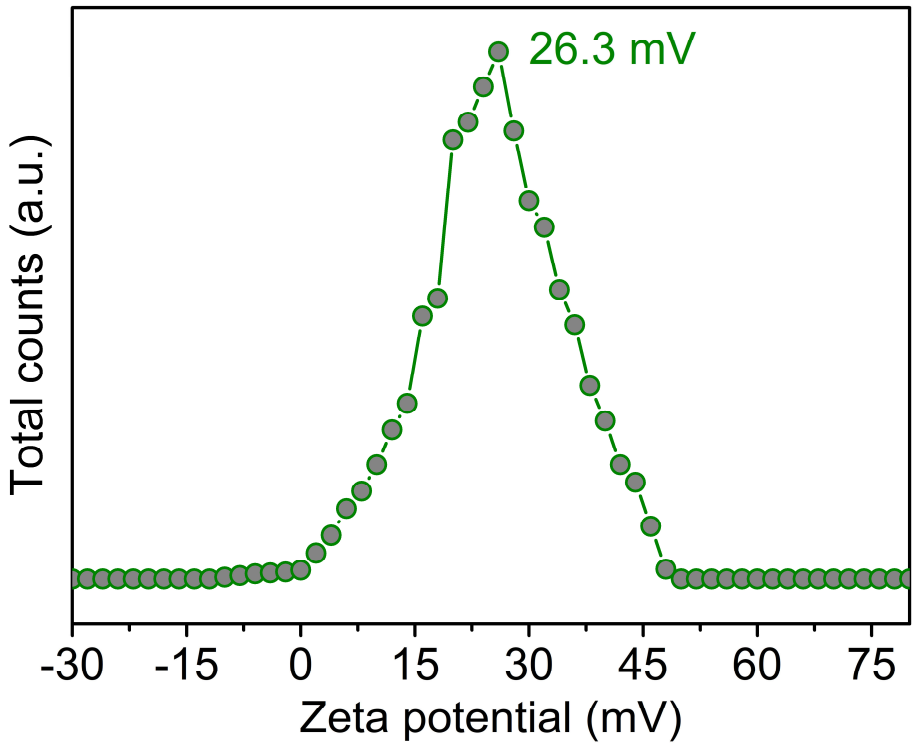

Fig. S10. Zeta potential distributions for the NiFe LDH from obtained *sd*-NFF electrodes.

The surface charge of NiFe LDH from *sd*-NFF electrode is investigated by Zeta potential test.

First, we prepare 40 pieces of *sd*-NFF electrodes. Due to the excellent mechanical stability of the NiFe LDH film on NFF, only 4.8 mg NiFe LDH powder are scraped off from NFF substrates and collected together. The powder is added in 250 mL water to get an aqueous solution ($C_{NiFe\ LDH}$=19.2 mg L^{-1}). The Zeta potential is measured at neutral condition to determine the charge on the surface of the sample.

Fig. S10 displays the distribution curves of the Zeta potential for NiFe LDH, with measured average values of 26.3 mV. Therefore, the surface of NiFe LDH carries positive charges at neutral condition. This result is consistent with previous reported ones.[9, 10]

Tab. S1. The inductively coupled plasma (ICP) results for the NiFe LDH from obtained *sd*-NFF electrodes.

Element	Sample	Concentration (mg L^{-1})	Mean concentration (mg L^{-1})
Ni	Sample #1	0.0016	0.0017
	Sample #2	0.0014	
	Sample #3	0.0021	
Fe	Sample #1	0.0008	0.0005
	Sample #2	0.0003	
	Sample #3	0.0004	

The surface element distribution of NiFe LDH from *sd*-NFF is further investigated by an inductively coupled plasma atom emission spectroscopy (ICP-AES) instrument.

We prepared 60 pieces of *sd*-NFF electrodes. 7.3 mg NiFe LDH powder are scraped off from NFF substrates and then collected together for the multi-element analysis. As shown in Tab. S1, the tests are repeated for three times (named as Sample #1, Sample #2, and Sample #3). The mean concentrations for Ni and Fe are 0.0017 and 0.0005 mg L^{-1}, respectively. Thus, the mole ratio for Ni:Fe can be calculated to be about 3.24:1.

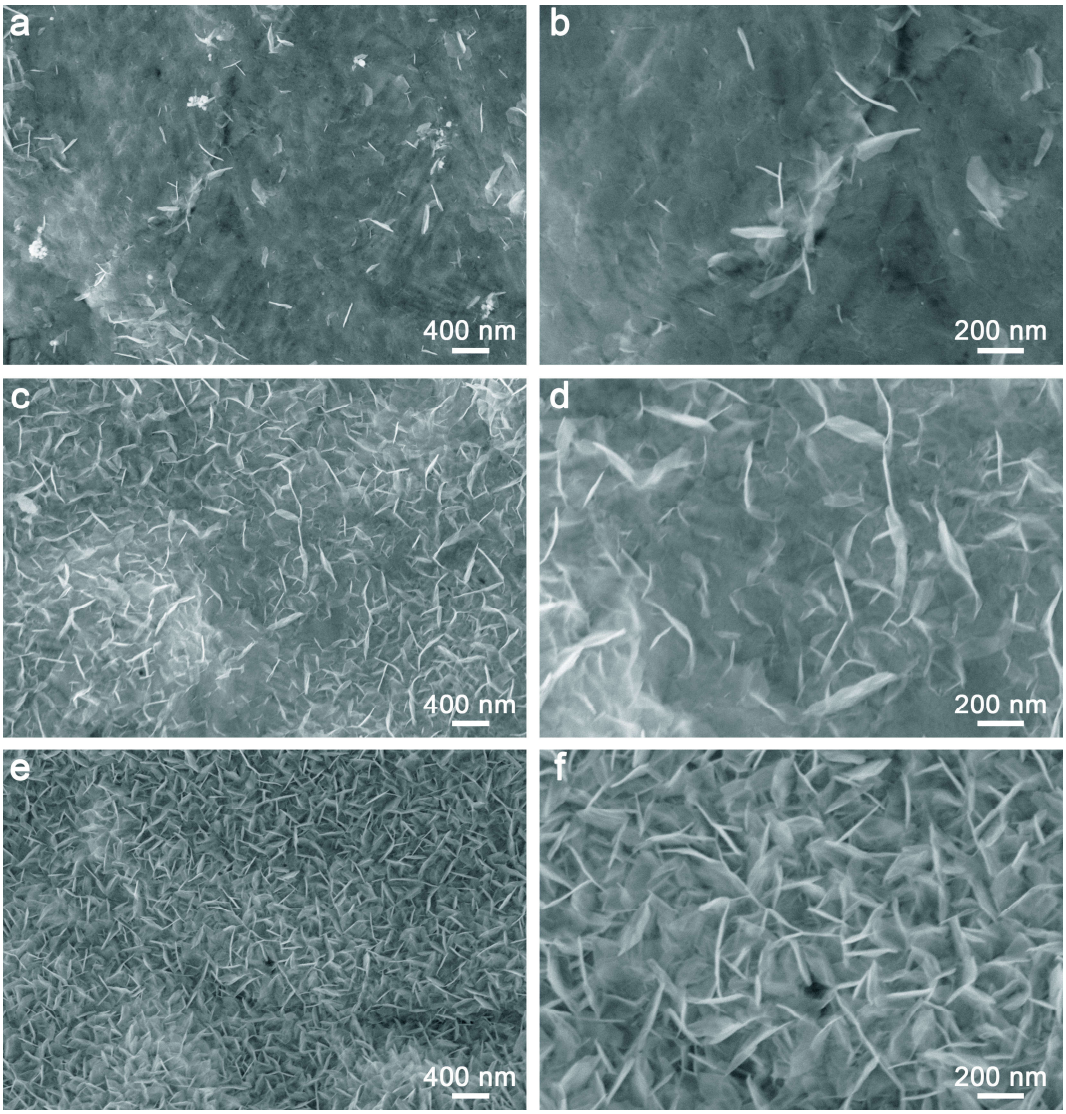

Fig. S11. Typical SEM images of *sd*-NFF with different H_2O_2 addition amount: (a, b) 0 μL, (c, b) 500 μL, and (e, f) 1000 μL.

The formation reaction of NiFe LDH on the surface of NFF is thought to be the Eqn. 1:

$$Ni/Fe + H_2O + O_2 \rightarrow NiFe\ LDH \quad (1)$$

which consists of the following redox half-reactions:

$$Ni \rightarrow Ni^{2+} + 2e^- \quad (E^0 = -0.257\ V\ vs.\ SHE) \quad (2)$$

$$Fe \rightarrow Fe^{3+} + 3e^- \quad (E^0 = -0.037\ V\ vs.\ SHE) \quad (3)$$

$$2H_2O + O_2 + 4e^- \rightarrow 4OH^- \quad (E^0 = 0.401\ V\ vs.\ SHE) \quad (4)$$

Since the standard electrode potential of Eqn. 4 is higher than that of Eqn. 2 and 3, O_2 is able to oxidize Ni/Fe to form NiFe LDH with the assistance of water as described by Eqn. 1. During the process, H_2O_2 keeps the reaction supplied with O_2 through a thermal decomposition (Eqn. 5):

$$2H_2O_2 \rightarrow 2H_2O + O_2 \quad (5)$$

According to the analyses above, H_2O_2 plays an important role in the growth of NiFe LDH. We have demonstrated the SEM images of those samples with different H_2O_2 addition amount (0, 500, and 1000 μL; Fig. S11). A 0 μL treatment leads to only sparse nanosheets on the NFF surface (Fig. S11 a, b). Increasing the H_2O_2 addition amount finally leads to a gradual growth of such nanosheets into ultrathin nanosheet arrays with several hundred nanometres in size (Fig. S11 c, d). However, the surface of NFF is still not completely covered with NiFe LDH until the H_2O_2 addition amount reaches to 750 μL (Fig. S17 a, c). Almost no change of coverage degree is observed when an even higher addition amount is involved (Fig. S11 e, f).

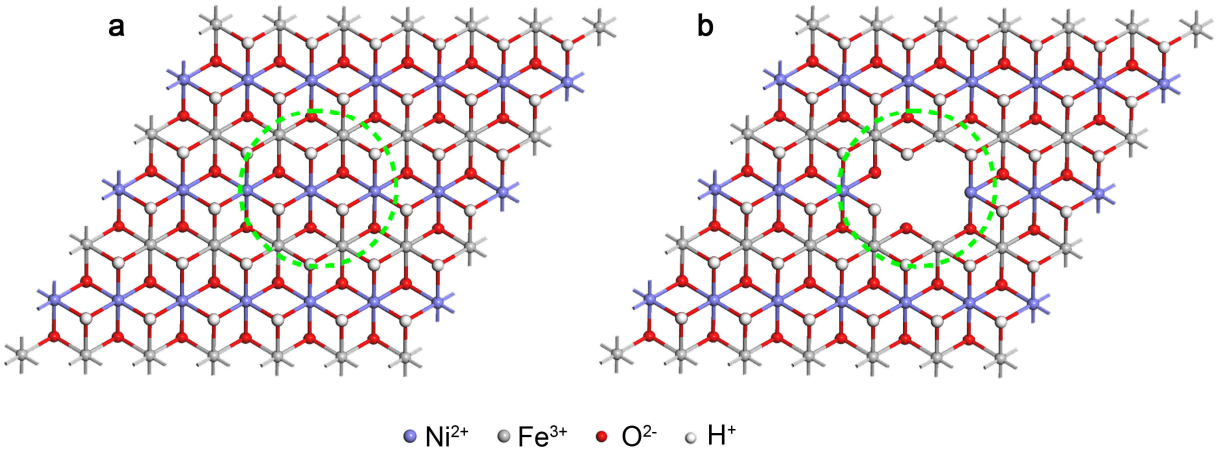

Fig. S12. Schematic illustration of single layer NiFe LDH (a) without and (b) with vacancies.

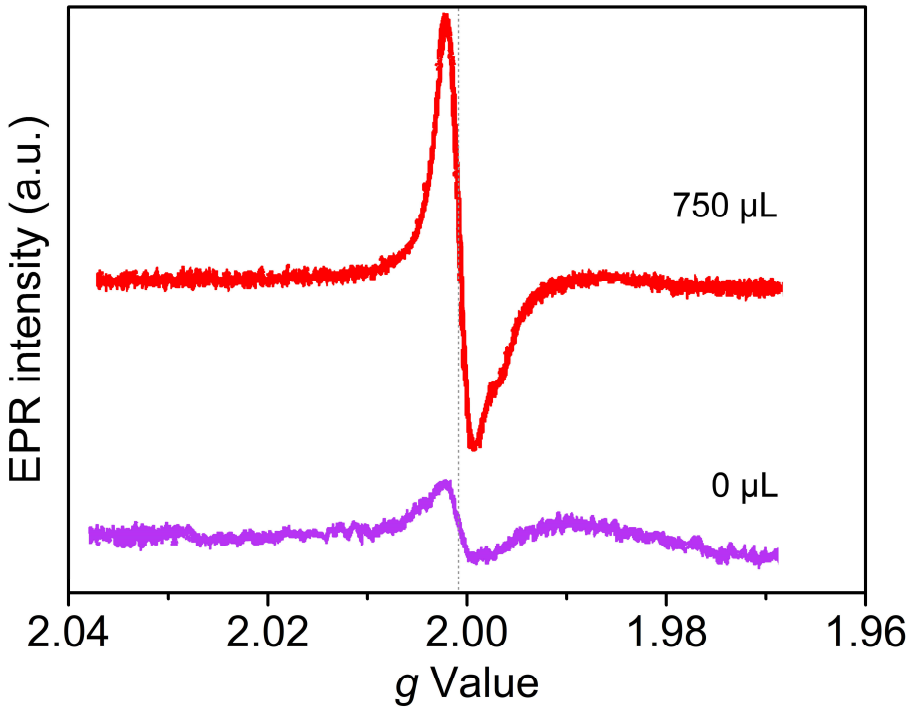

Fig. S13. EPR spectra of the *sd*-NFF electrodes prepared using 0 and 750 μL H_2O_2 additive.

According to the previous research,[11-13] the observed deletion of lattice orders (Fig. 3b and S6) is a typical crystal structure defect for 2D metal layered hydroxides, which is mainly aroused by the vacancy defects (as shown in Fig. S12).

Electron paramagnetic resonance (EPR) analysis is used to further verify the vacancies in NiFe LDH. As shown in Fig. S13, an obvious EPR signal appears at g=2.001, which could be identified as the electrons trapped on O vacancies.[11, 14, 15] Moreover, the as-prepared *sd*-NFF electrode with 750 μL H_2O_2 additive demonstrates much higher signal intensity than that of the sd-NFF electrode without using H_2O_2 additive, reasserting that the former has more O vacancy defects in the structure. This result is also consistent with the TEM characteristics (Fig. 3b, S6, and S7).

a

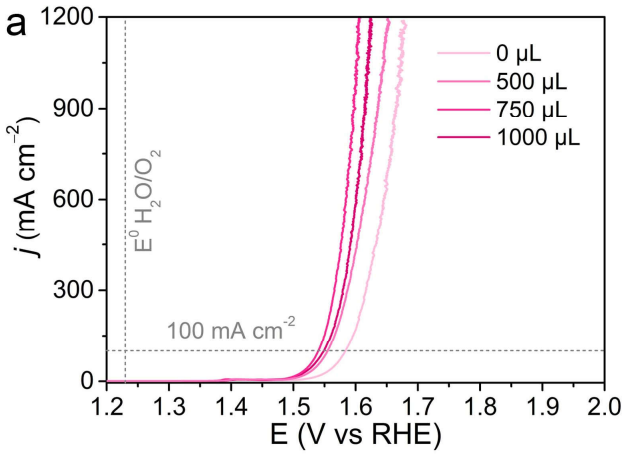

b

Amount of H_2O_2 additive (μL)	Performance indicators	
	η_{100} (mV)	j_{371} (mA cm^{-2})
0	354	176.4
500	325	436.4
750	310	1000
1000	319	608.5

Fig. S14. (a) LSV curves and (b) the corresponding OER properties of *sd*-NFF electrodes with H_2O_2 additive for different amount.

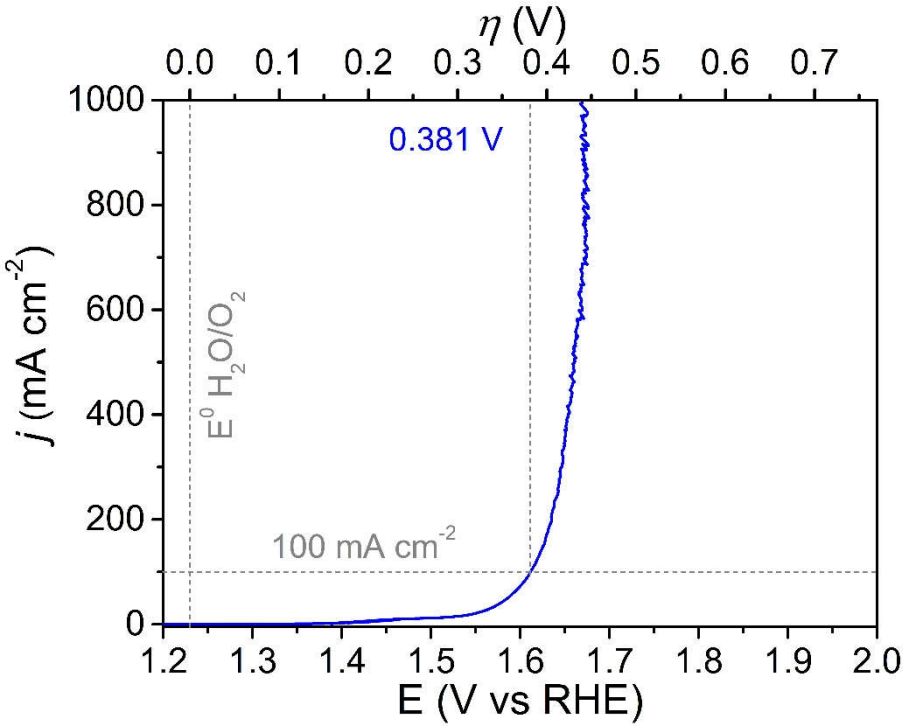

Fig. S15. OER polarization curve of RuO_2@NFF collected in 1 m KOH at a scan rate of 5 mV s^{-1}.

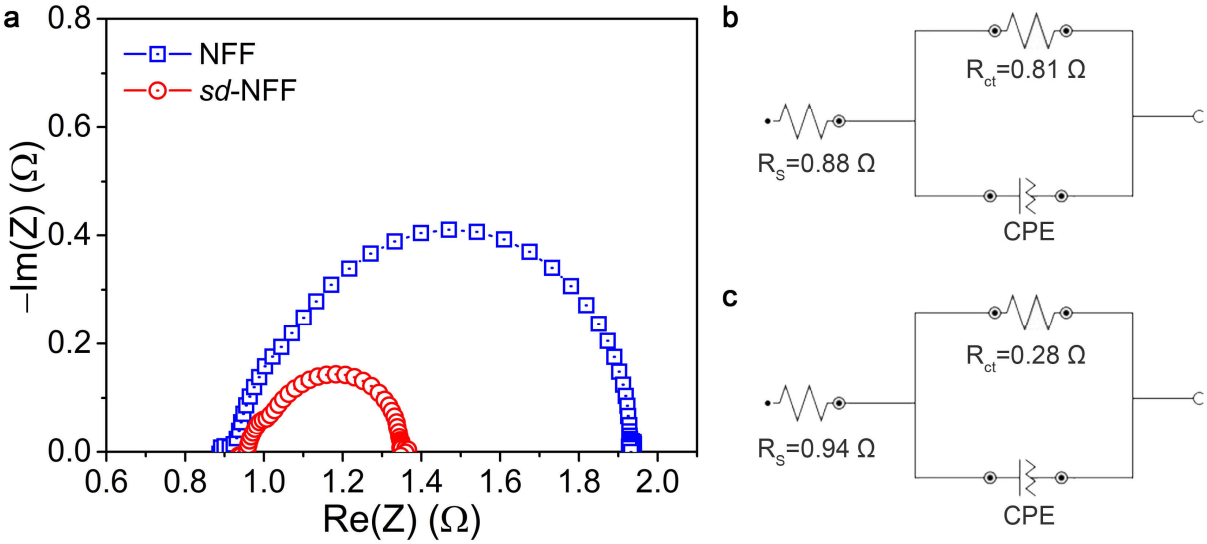

Fig. S16. (a) Nyquist plots at an overpotential of 280 mV. Electrical equivalent circuit used for fitting impedance spectra and the corresponding fitting results: (b)NFF and (c) *sd*-NFF. R_s: equivalent series resistance, R_{ct}: charge-transfer resistance, CPE: constant-phase element.

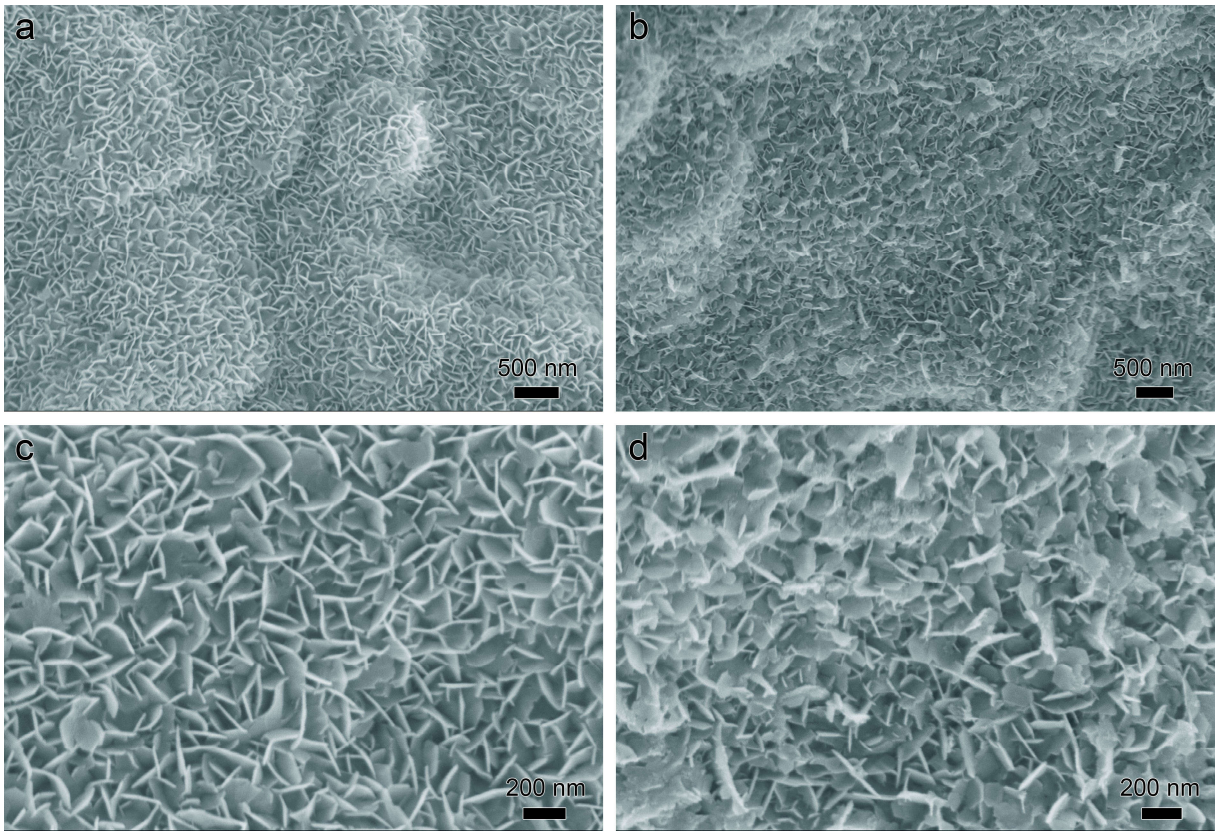

Fig. S17. Typical SEM images of *sd*-NFF (a, c) before and (b, d) after the chronopotentiometry measurement.

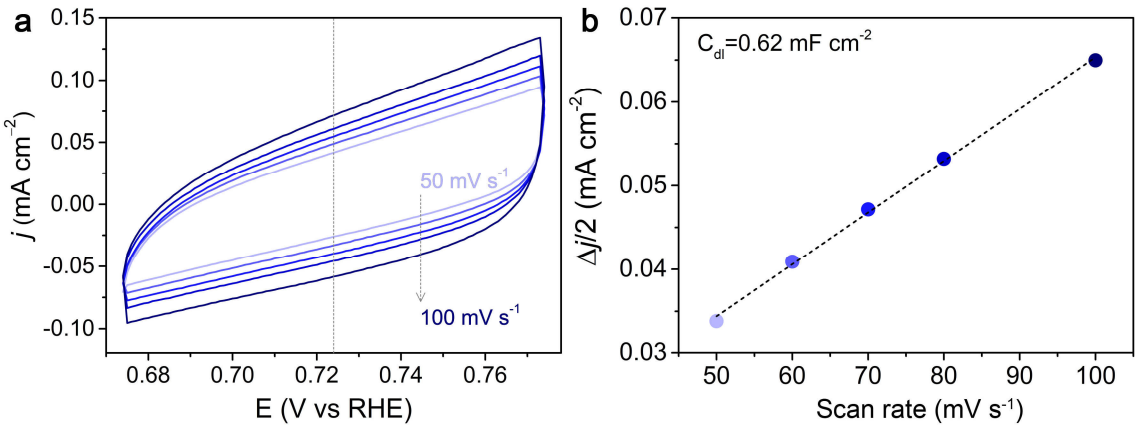

Fig. S18. Double-layer capacitance measurements for determining the ESCA of NFF from CV scans performed in 1 M KOH. (a) CV plots were measured in a non-Faradaic region of the voltammogram at the following scan rate: 50, 60, 70, 80, and 100 mV s^{-1}. (b) The corresponding linear fitting of the capacitive currents with respect to scan rates. The calculated C_{dl} value is shown in the upper-left corner of (b).

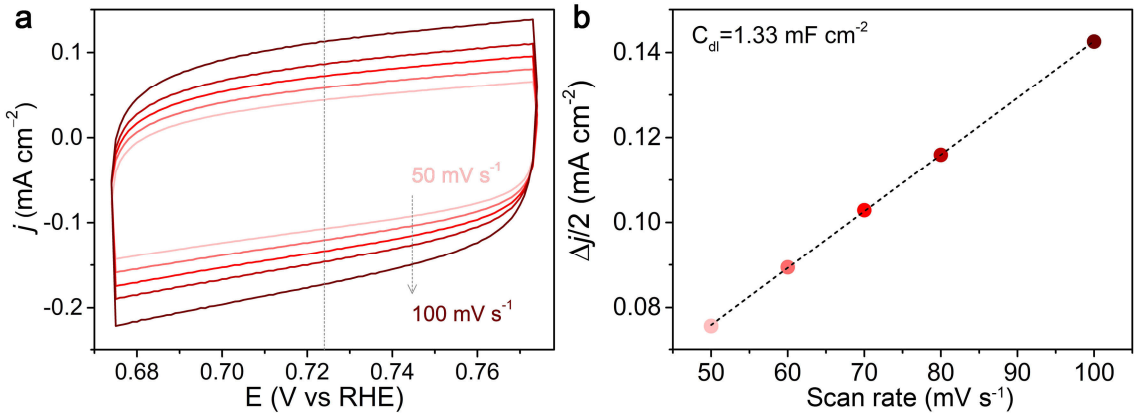

Fig. S19. Double-layer capacitance measurements for determining the ESCA of *sd*-NFF from CV scans performed in 1 M KOH. (a) CV plots were measured in a non-Faradaic region of the voltammogram at the following scan rate: 50, 60, 70, 80, and 100 mV s^{-1}. (b) The corresponding linear fitting of the capacitive currents with respect to scan rates. The calculated C_{dl} value is shown in the upper-left corner of (b).

In our work, the BET specific area of the samples is very hard to test. First, *sd*-NFF is a metal-foam-based monolithic electrode, whose BET surface could be as low as 0.01~0.155 m^2 g^{-1}.[16] Therefore, it is difficult to get an accurate value using common surface area and porosity analyzers. Second, the mass loading of NiFe LDH nanosheets on *sd*-NFF electrode is only ~0.23 mg cm^{-2}. And the strong adhesion of catalysts on the electrode make it difficult to collect at least dozens of milligrams for the BET surface test.

Herein, we investigate the specific area of NiFe LDH nanosheets on *sd*-NFF electrode through an electrochemical measurement.[5] The double-layer capacitance (C_{dl}) is directly used to estimate the relevant specific surface area by using the specific capacitance value for a flat electrode with real surface area 1 cm^2. We assumed 40 μF cm^{-2} for a flat electrode provided in Jaramillo et al[3, 4] and Kim et al[17] for calculation here. The NiFe LDH loading (m) on the NFF electrode is about 0.23 mg cm^{-2}. The C_{dl} value for *sd*-NFF is 1.33 mF cm^{-2}. Thus, the specific surface area (S) of NiFe LDH can be calculated as follows:

$$S=\frac{A}{m}=\frac{1.33\times1000/40/10000}{0.23/1000}\,m^2/g\approx14.46\,m^2/g$$

The specific surface area of NiFe LDH nanosheets on *sd*-NFF electrode can be approximately considered to be 14.46 m^2 g^{-1}.

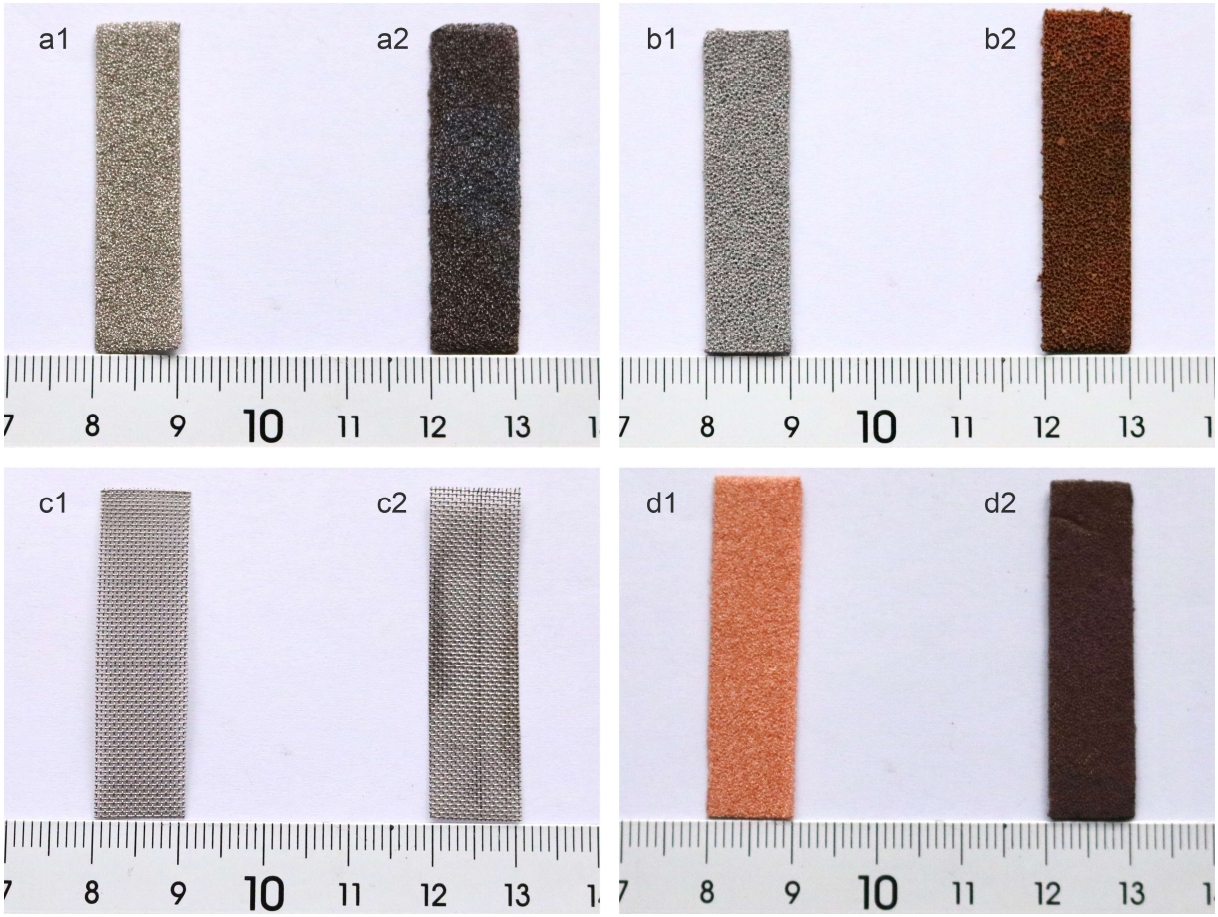

Fig. S20. Photograph of (a1) bare NF, (a2) *sd*-NF, (b1) bare FF, (b2) *sd*-FF, (c1) bare SSM, (c2) *sd*-SSM, (d1) bare CF, and (d2) *sd*-CF.

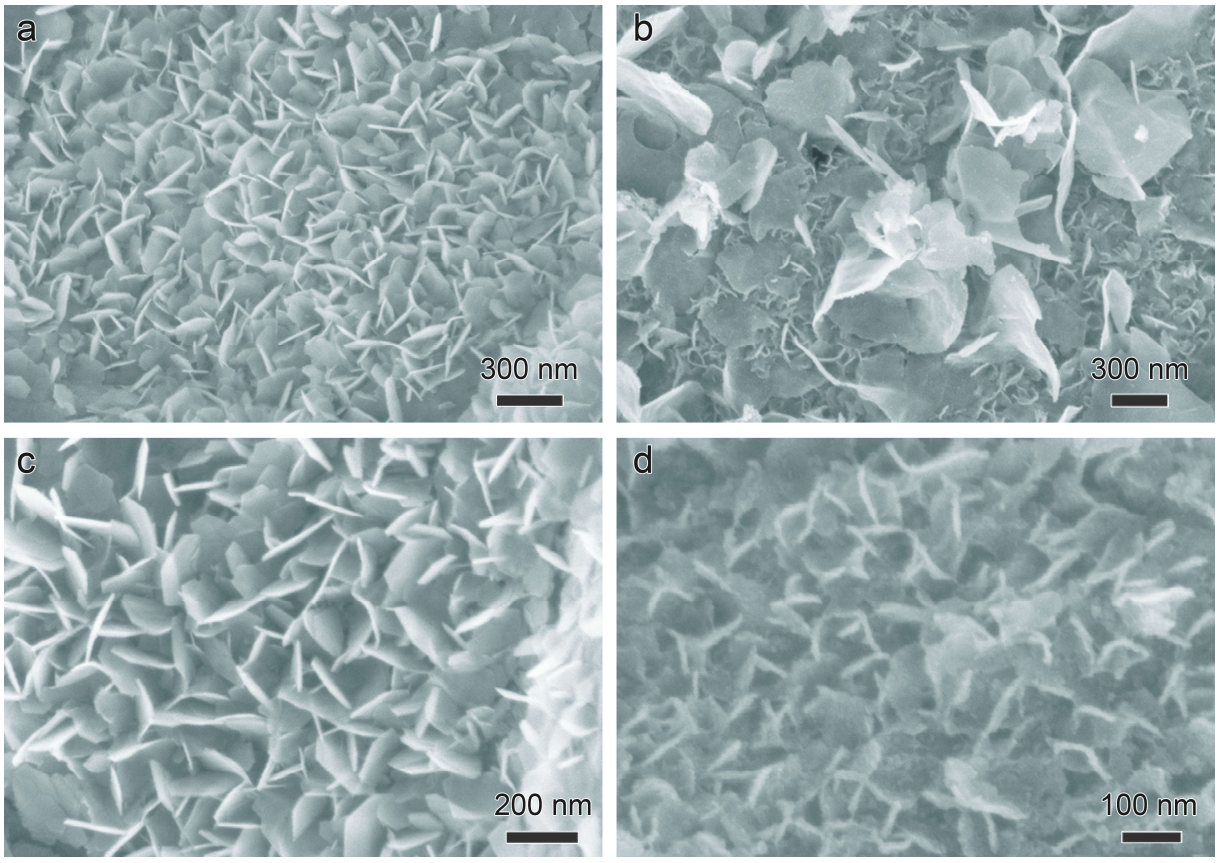

Fig. S21. SEM images of (a) *sd*-NF, (b) *sd*-FF, (c) *sd*-SSM, and (d) *sd*-CF, respectively.

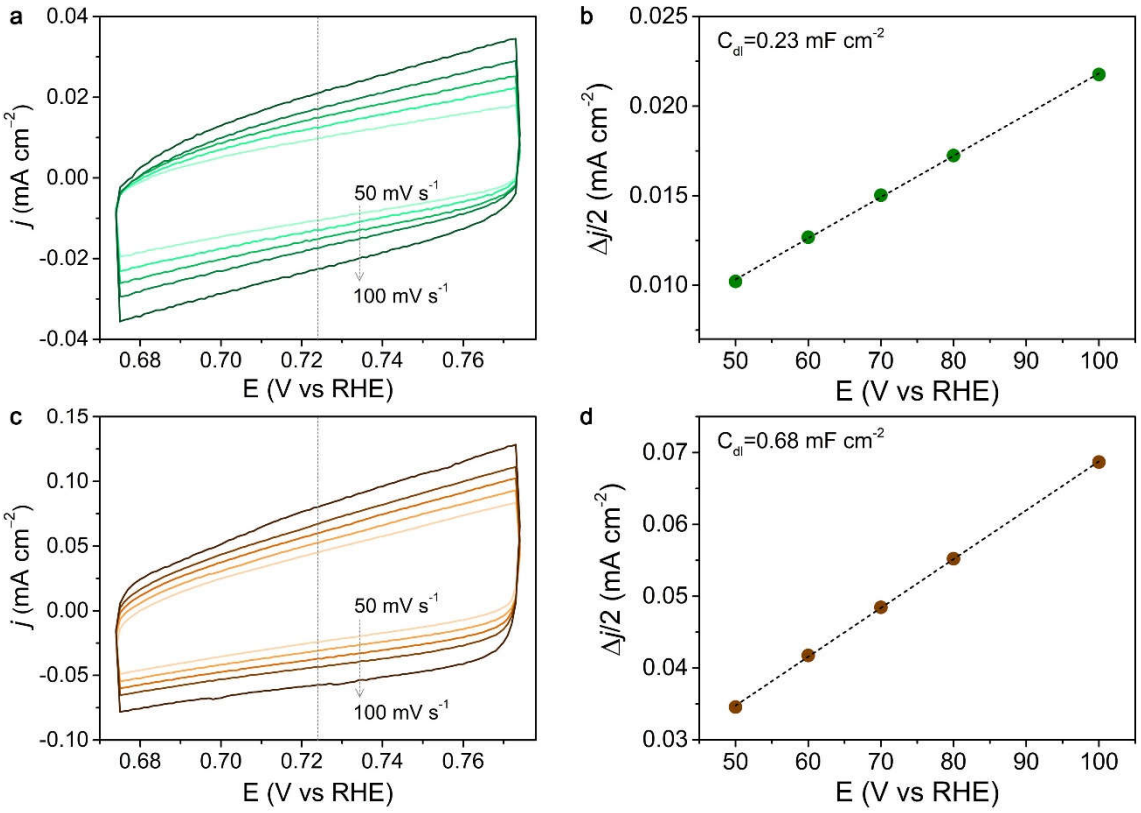

Fig. S22. Cyclic voltammograms at 50, 60, 70, 80, and 100 mV s^{-1}, and the corresponding linear fitting of the capacitive currents with respect to scan rates: (a, b) NF, (c, d) *sd*-NF. The calculated C_{dl} values are shown in the upper-left corner of (b) and (d) for NF and *sd*-NF, respectively.

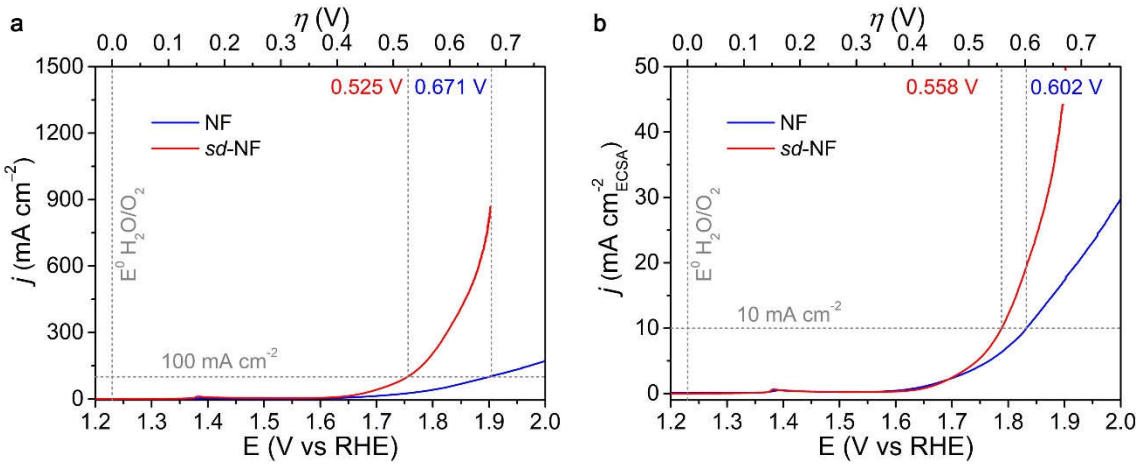

Fig. S23. (a) OER polarization curves and (b) ECSA-normalized OER polarization curves of the NF and *sd*-NF electrodes, respectively.

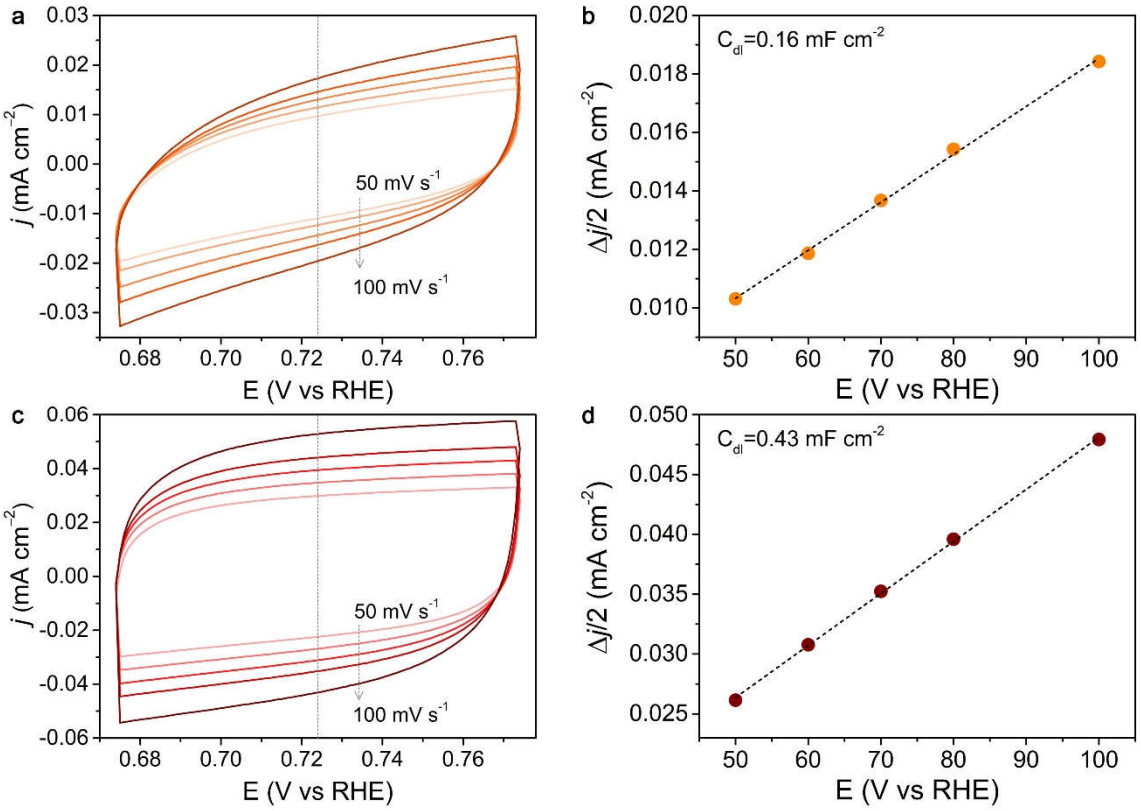

Fig. S24. Cyclic voltammograms at 50, 60, 70, 80, and 100 mV s^{-1}, and the corresponding linear fitting of the capacitive currents with respect to scan rates: (a, b) FF, (c, d) *sd*-FF. The calculated C_{dl} values are shown in the upper-left corner of (b) and (d) for FF and *sd*-FF, respectively.

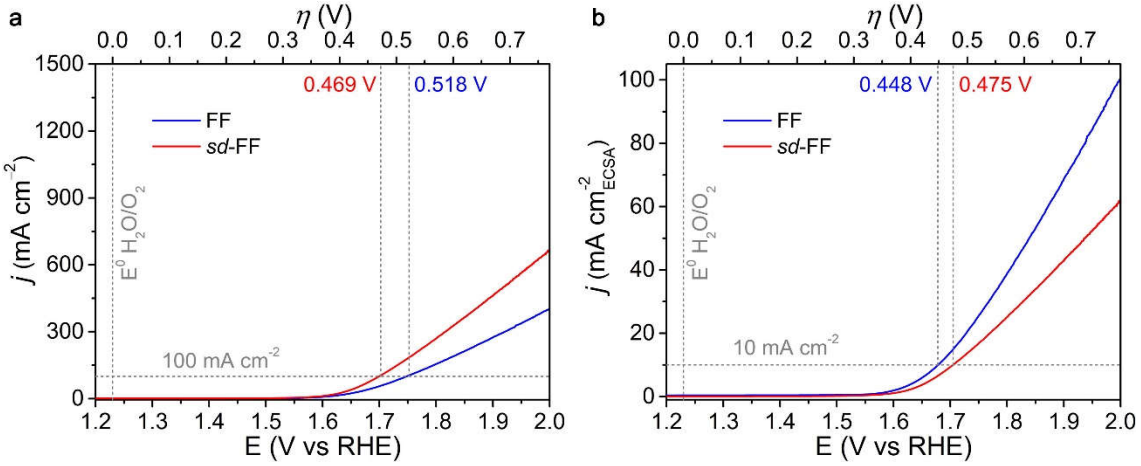

Fig. S25. (a) OER polarization curves and (b) ECSA-normalized OER polarization curves of the FF and *sd*-FF electrodes, respectively.

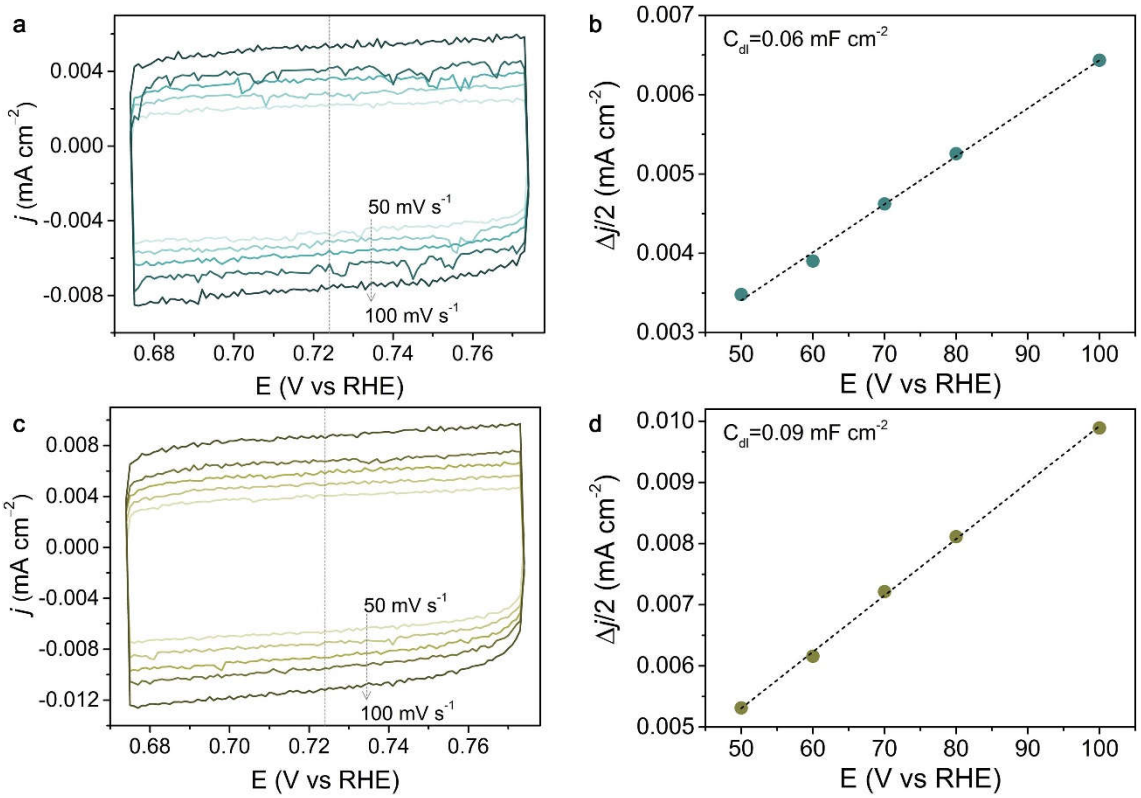

Fig. S26. Cyclic voltammograms at 50, 60, 70, 80, and 100 mV s^{-1}, and the corresponding linear fitting of the capacitive currents with respect to scan rates: (a, b) SSM, (c, d) *sd*-SSM. The calculated C_{dl} values are shown in the upper-left corner of (b) and (d) for SSM and *sd*-SMM, respectively.

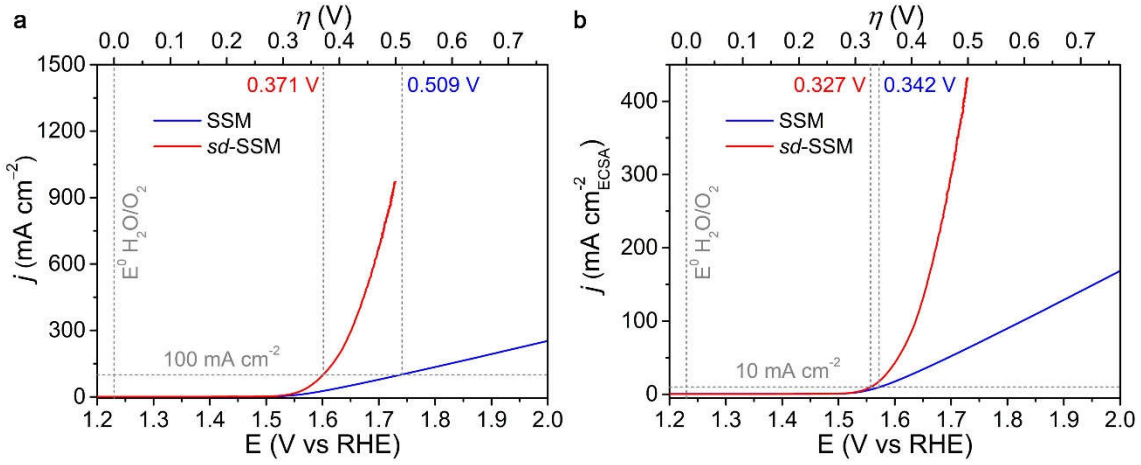

Fig. S27. (a) OER polarization curves and (b) ECSA-normalized OER polarization curves of the SSM and *sd*-SSM electrodes, respectively.

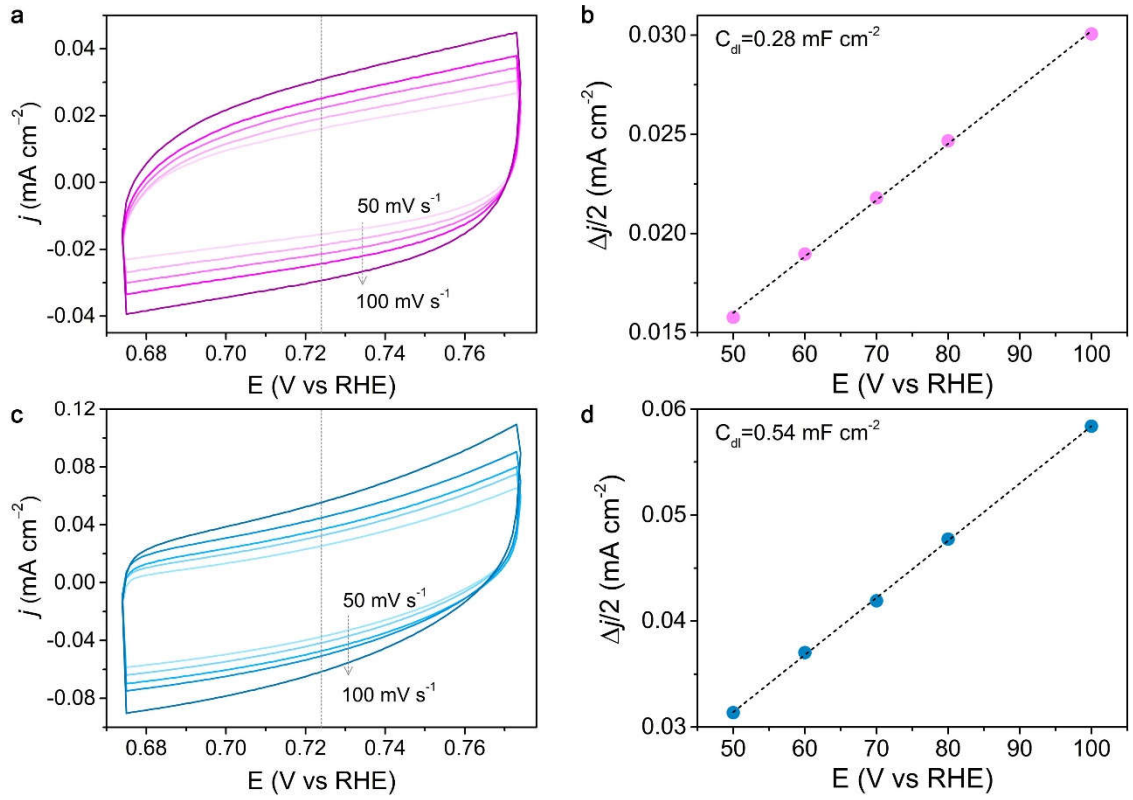

Fig. S28. Cyclic voltammograms at 50, 60, 70, 80, and 100 mV s^{-1}, and the corresponding linear fitting of the capacitive currents with respect to scan rates: (a, b) CF, (c, d) *sd*-CF. The calculated C_{dl} values are shown in the upper-left corner of (b) and (d) for CF and *sd*-CF, respectively.

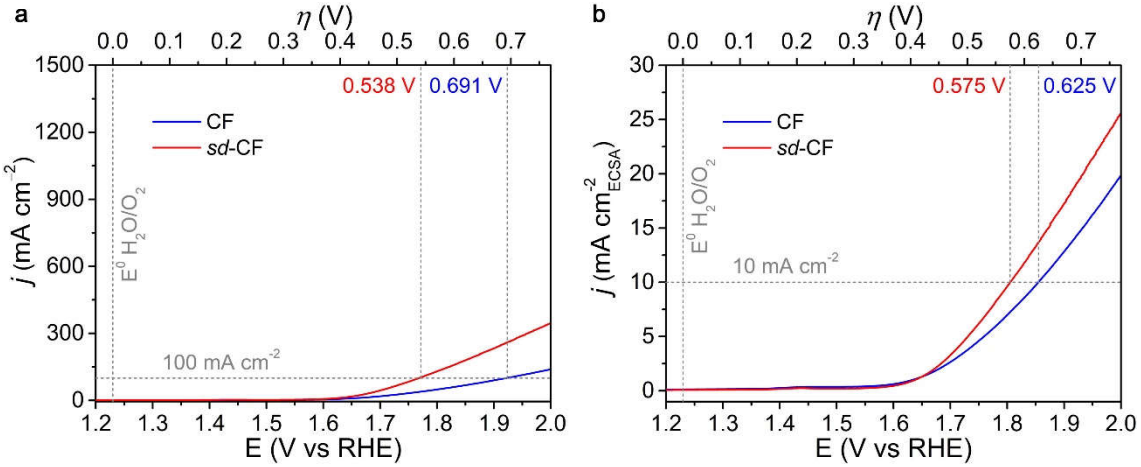

Fig. S29. (a) OER polarization curves and (b) ECSA-normalized OER polarization curves of the CF and *sd*-CF electrodes, respectively.

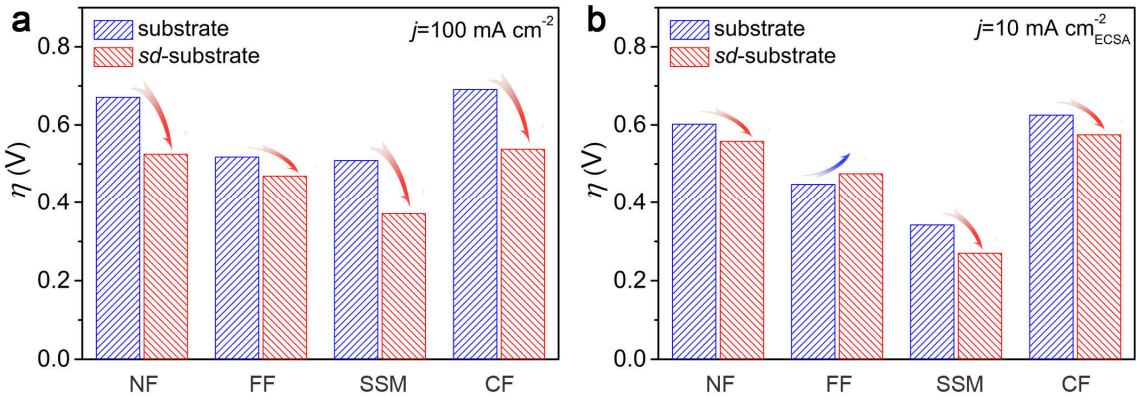

Fig. S30. Comparison of the overpotentials for NF, FF, SSM, and CF samples before (substrate) and after (*sd*-substrate) the self-derivation-behaviour: (a) η_{100} at the corresponding current density normalized by geometric area of electrode; (b) η_{10} at the corresponding current density normalized by ECSA of electrode.

Tab. S2. OER performances of *sd*-NFF and other reported electrocatalysts in 1.0 M KOH. (*j*: current density; *η*: overpotential).

Electrode	η (mV) @j=100 mA cm^{-2}	j (mA cm^{-2}) @η=371 mV	Tafel slope (mV dec^{-1})	References
sd-NFF	310	1000	49	This work
Boronized Ni plate	~350	N/A	47	[18]
FeNiOH/NF	320	~350	72	[19]
NiFe/NiSx-Ni foam	~370	~100	N/A	[20]
Ni-NM@G	318	<300	N/A	[21]
Fe-NM@G	400	<100	N/A	
Activated stainless steel plate	~314	~350	32	[22]
Fe-Ni_3S_2/FeNi	~470	~50	54	[23]
Co_2P/Co-Foil	>470	~30	79	[24]
pa-NiFe LDH NS/NIF	326	<100	157	[25]
FeNi@FeNiB-700	400	~75	136	[26]
Ni-Fe-OH@Ni_3S_2/NF	300	~250	93	[27]
Fe:Ni/Ni_2P inverse opal	380	N/A	54	[5]

References

1. W. Zhu, T. Zhang, Y. Zhang, Z. Yue, Y. Li, R. Wang, Y. Ji, X. Sun and J. Wang, *Applied Catalysis B: Environmental*, 2019, **244**, 844-852.
2. J. Kibsgaard and T. F. Jaramillo, *Angewandte Chemie International Edition*, 2014, **53**, 14433-14437.
3. J. Kibsgaard, Z. Chen, B. N. Reinecke and T. F. Jaramillo, *Nature Materials*, 2012, **11**, 963-969.
4. J. D. Benck, Z. Chen, L. Y. Kuritzky, A. J. Forman and T. F. Jaramillo, *ACS Catalysis*, 2012, **2**, 1916-1923.
5. Q. Zhou, J. Pu, X. Sun, C. Zhu, J. Li, J. Wang, S. Chang and H. Zhang, *Journal of Materials Chemistry A*, 2017, **5**, 14873-14880.
6. J. Li, C. Zhang, T. Zhang, Z. Shen, Q. Zhou, J. Pu, H. Ma, T. Wang, H. Zhang, H. Fan, Y. Wang and H. Ma, *Chemical Engineering Journal*, 2020, **397**, 125457.
7. L. Yu, J. F. Yang, B. Y. Guan, Y. Lu and X. W. Lou, *Angewandte Chemie International Edition*, 2018, **57**, 172-176.
8. F. Liu, X. Chu, H. Zhang, B. Zhang, H. Su, L. Jin, Z. Wang, H. Huang and W. Yang, *Electrochimica Acta*, 2018, **269**, 102-110.
9. Y. Zheng, B. Cheng, W. You, J. Yu and W. Ho, *Journal of Hazardous Materials*, 2019, **369**, 214-225.
10. Y. Han, P. Li, J. Liu, S. Wu, Y. Ye, Z. Tian and C. Liang, *Scientific Reports*, 2018, **8**, 1359.
11. C. Yan, Z. Fang, C. Lv, X. Zhou, G. Chen and G. Yu, *ACS Nano*, 2018, **12**, 8670-8677.
12. J. Xie, X. Zhang, H. Zhang, J. Zhang, S. Li, R. Wang, B. Pan and Y. Xie, *Advanced Materials*, 2017, **29**, 1604765.
13. Z. Liu, Z. Zhao, Y. Wang, S. Dou, D. Yan, D. Liu, Z. Xia and S. Wang, *Advanced Materials*, 2017, **29**, 1606207.
14. S.-M. Wu, X.-L. Liu, X.-L. Lian, G. Tian, C. Janiak, Y.-X. Zhang, Y. Lu, H.-Z. Yu, J. Hu, H. Wei, H. Zhao, G.-G. Chang, G. Van Tendeloo, L.-Y. Wang, X.-Y. Yang and B.-L. Su, *Advanced Materials*, 2018, **30**, 1802173.
15. H. Yu, J. Li, Y. Zhang, S. Yang, K. Han, F. Dong, T. Ma and H. Huang, *Angewandte Chemie International Edition*, 2019, **58**, 3880-3884.
16. S. Langlois and F. Coeuret, *Journal of Applied Electrochemistry*, 1989, **19**, 43-50.
17. D. J. Li, U. N. Maiti, J. Lim, D. S. Choi, W. J. Lee, Y. Oh, G. Y. Lee and S. O. Kim, *Nano Letters*, 2014, **14**, 1228-1233.
18. J. Li, H. Chen, Y. Liu, R. Gao and X. Zou, *Journal of Materials Chemistry A*, 2019, **7**, 5288-5294.
19. J.-T. Ren, G.-G. Yuan, C.-C. Weng, L. Chen and Z.-Y. Yuan, *Nanoscale*, 2018, **10**, 10620-10628.
20. Y. Kuang, M. J. Kenney, Y. Meng, W.-H. Hung, Y. Liu, J. E. Huang, R. Prasanna, P. Li, Y. Li, L. Wang, M.-C. Lin, M. D. McGehee, X. Sun and H. Dai, *Proceedings of the National Academy of Sciences*, 2019, **116**, 6624.
21. J. Zhang, W.-J. Jiang, S. Niu, H. Zhang, J. Liu, H. Li, G.-F. Huang, L. Jiang, W.-Q. Huang, J.-S. Hu and W. Hu, *Advanced Materials*, 2020, **32**, 1906015.
22. H. Zhong, J. Wang, F. Meng and X. Zhang, *Angewandte Chemie International Edition*, 2016, **55**, 9937-9941.
23. C.-Z. Yuan, Z.-T. Sun, Y.-F. Jiang, Z.-K. Yang, N. Jiang, Z.-W. Zhao, U. Y. Qazi, W.-H. Zhang and A.-W. Xu, *Small*, 2017, **13**, 1604161.
24. C.-Z. Yuan, S.-L. Zhong, Y.-F. Jiang, Z. K. Yang, Z.-W. Zhao, S.-J. Zhao, N. Jiang and A.-W. Xu, *Journal of Materials Chemistry A*, 2017, **5**, 10561-10566.

25. J. Xie, H. Qu, F. Lei, X. Peng, W. Liu, L. Gao, P. Hao, G. Cui and B. Tang, *Journal of Materials Chemistry A*, 2018, **6**, 16121-16129.
26. H. Yuan, S. Wang, X. Gu, B. Tang, J. Li and X. Wang, *Journal of Materials Chemistry A*, 2019, **7**, 19554-19564.
27. X. Zou, Y. Liu, G.-D. Li, Y. Wu, D.-P. Liu, W. Li, H.-W. Li, D. Wang, Y. Zhang and X. Zou, *Advanced Materials*, 2017, **29**, 1700404.